Lawrence Berkeley National Laboratory

Title
In Situ Scanning Electron Microscopy Analysis of the Interfacial Failure of Oxide Scales on Stainless Steels and Its Effect on Sticking during Hot Rolling.

Permalink
https://escholarship.org/uc/item/5gm1p158

Authors
Lee, Soyeon

Kim, Seung-Rok

Triambulo, Ross

et al.

Peer reviewed

In Situ Scanning Electron Microscopy Analysis of the Interfacial Failure of Oxide Scales on Stainless Steels and Its Effect on Sticking during Hot Rolling

Soyeon Lee,[∥,⊥] Seung-Rok Kim,[∥] Ross E. Triambulo,[⊥] Chang-Jin Lim,[⊥] Han-Jin Kim, Jin-Yoo Suh, Hyung-Gu Kang, and Jin-Woo Park*[,⊥]

ACCESS | Metrics & More | Article Recommendations | SI Supporting Information

ABSTRACT: Despite various strategies to address sticking failure in stainless steels (STSs), difficulties in understanding its fundamental mechanisms hinder precise solutions during STS fabrication. This study investigated the effect of chromium (Cr) content on the microstructures and failure modes of oxide scales under a tensile load, simulating the hot-rolling process. The dynamic, real-time behavior of crack initiation, propagation, and interfacial delamination in the oxide scales under tension was analyzed using an *in situ* scanning electron microscopy (SEM) tensile test. With a high Cr content, iron (Fe) oxide and chromium(III) oxide (Cr_2O_3) form a layered structure, which is delaminated along the interfaces between the thin Cr_2O_3 layer and the bulk after perpendicular cracking. The saturated crack densities obtained from *in situ* SEM provide interfacial strength, while the elastic modulus and hardness obtained from nanoindentation provide vertical fracture strength. In combination with an *ex situ* elemental image analysis, the *in situ* SEM results reveal three different failure modes of the four different STSs. The results confirm that sticking failure is more likely to occur as the Cr content increases.
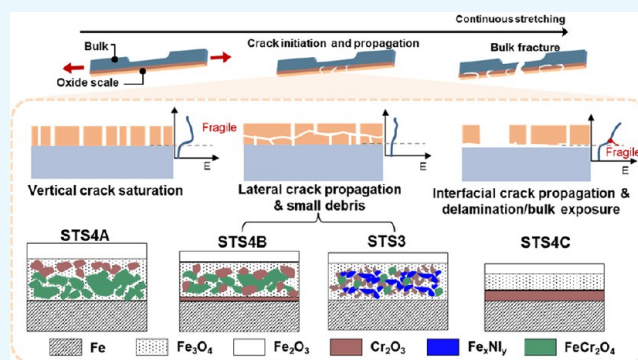
1. INTRODUCTION

Stainless steels (STSs) have a wide range of applications, from kilometer-scale structural components to nanometer-scale electronic devices.[1] The mechanical and chemical robustness in harsh environments, cost effectiveness, and processability of STSs can be controlled by changing their composition.[2,3] A slight difference in composition can transform the STS phases among ferrite, austenite, and martensite, which have different microstructures and mechanical properties.[2−4] STSs with a high chromium (Cr) content (11−30 wt %) and minimal amounts of other elements have a ferritic body-centered cubic structure, whereas STSs containing nickel (Ni) have an austenitic face-centered cubic structure.[3]

STSs with low and medium Cr contents are martensite.[3] Austenitic STSs have high mechanical stability, corrosion resistance, and formability over a wide temperature range.[3,5,6] However, ferritic STSs have been preferred over martensite and austenitic STSs due to the high cost of Ni.[7] Highly purified, microalloyed ferritic STSs have been developed as a counterpart to austenitic STSs to improve the corrosion resistance and mechanical properties of ferritic STSs with a Cr content of more than 18−19 wt %.[7]

However, during the hot rolling of ferritic STSs with a high Cr content, oxide flakes form and stick to the rollers,[4]

deteriorating the surface of the STSs.[8,9] Because the surface quality is critical, STSs with indented surfaces have significantly diminished value.[10,11] Therefore, many engineers have tried to explain the fundamental mechanisms[12,13] and address the sticking failure problem with empirical control of alloying elements,[9] structural analysis,[11] processing parameter controls,[10] and replication of hot-rolling processes.[14] Kim et al.[15] suggested failure mechanisms with different types of commercial STSs on the basis of an *ex situ* elemental image analysis of the microstructure of the scale and the exposed fractured surface. However, a real-time investigation of sticking failure is required to determine the failure process in terms of the crack initiation position, preferable cracking path, and delamination.

In situ, continuous monitoring of scale failure processes can facilitate a closer inspection of the sticking mechanism during

the hot-rolling process.[16] Scanning electron microscopy (SEM) is used to investigate the *in situ* dynamics of sticking failure because it is commonly used to study the mechanical resistance of brittle coatings on ductile substrates to external tensile loads.[17−21] Researchers have used *in situ* micrographs to explain the process of oxide failure in terms of the dependence of the crack spallation spacing on oxide scale thickness.[17,20,22,23] Furthermore, most studies have focused on describing the failure mechanisms at the interface region between a ductile metal and the brittle oxide scale, exploring the mechanisms with limited types of STSs.[17,18,23] However, to the best of our knowledge, none have investigated the effect of the mechanical properties of each microstructure on sticking failure due to the oxide scale—either in the form of a composite or in layers—with various elemental ratios in STSs.[15,24,25]

This study investigated the sticking failure mechanism of four different STSs with different Cr contents on the basis of the fracture patterns of the oxide scales formed on STSs under tension. The lowest Cr content was 11 wt %, and the highest was 21 wt %. The dynamic response of oxide scales obtained from an *in situ* SEM tensile test validated the exposed microstructure under a tensile test at high temperature (Gleeble test). In the test, real-time crack initiation, propagation, and delamination of the oxide scales occurred as the strain was increased to 10%. The microstructure and mechanical properties were analyzed by an *ex situ* elemental image analysis using electron probe microanalysis (EPMA) and nanoindentation, respectively. The *in situ* SEM tensile results were analyzed based on the microstructural composition and mechanical properties of the oxide scales. On the basis of the interpretation of the superiority between interfacial strength and vertical fracture strength in the four different STSs, the sticking failure modes depend primarily on the interfacial microstructural composition of each STS. On the basis of the *ex situ* and *in situ* analyses of the four STSs, the critical effect of Cr content on the sticking problem can be observed.

2. EXPERIMENTAL SECTION

2.1. Chemical Compositions of STSs. The names and chemical compositions (wt %) of the four types of STS alloys are summarized in Table 1. STS4A, STS4B, and STS4C are

Table 1. Names and Chemical Compositions (wt %) of Ferritic and Austenitic STSs[a]

sample name	Fe	Cr	Ni	C	Ti
STS4A	balance	11	0	≤0.01	0.05
STS4B	balance	18	0	≤0.01	0.06
STS4C	balance	21	0	≤0.01	≤0.4
STS3	balance	18	8	≤0.05	0.04

[a]Other elements, including Si, Mn, W, Mo, Nb, P, and S, exist in quantities less than 1 wt %.

ferritic STSs with 11, 18, and 21 wt % Cr contents, respectively. None of the STS4 series contained Ni. STS3 is an austenitic STS with 18 wt % Cr content and 8 wt % Ni content. A minimal quantity of other elements, such as C, Ti, Si, Mn, W, Mo, Nb, Ti, C, P, and S (less than 1 wt %), can be used for various purposes, including oxidation control, corrosion resistance, and formability.[3] Typically only STS3 contains Mn with 0.96 wt %, while other STSs do not. In this study, we focused on the characteristic content of Cr and the

presence of Ni to analyze the effects of the mechanical properties on the sticking problem.

2.2. Sample Preparation. The STSs in Table 1 were oxidized for 2 h at 1200 °C under atmospheric pressure and pressed by roughening and finishing rolls at 1000 °C in a commercial production plant. At every interval of each step, descaling of the outermost oxide scales of STSs was performed frequently with a high-pressure hydraulic descaler, as described in a previous study.[15] According to the product statistics confirmed by visual detection, STS4C has suffered sticking failures most frequently among the four types of STSs given in Table 1, implying that the fracture pattern of oxide scales formed on high-Cr-content STSs during hot rolling differs significantly from that of oxide scales formed on the other STSs presented in the table.

2.3. Gleeble Test. To mimic the stress conditions during hot rolling experienced by the oxide scales, we conducted a thermomechanical tensile test through a Gleeble test setup (Gleeble 3800, Imdea Materials). The oxide scales can be simultaneously examined under vertical compression and horizontal tension, resulting in the bare bulk STS exposure. All samples were stretched to 20% strain with a fixed strain rate of 1 s⁻¹ under a 950 °C ambient atmosphere. Accurate control of the specimen temperature was carried out using temperature feedback signals predicted by thermocouples. The compound types on the exposed top surface of these Gleeble samples were compared, which provides direct information regarding sticking failure.

2.4. Measurements. Nanoindentation is an experiment that involves indenting the surfaces of materials with an ultralow load[26] using a nanoindenter (TI-950, Bruker). We used a trigonal (Berkovich) tip, and a 10 mN load was applied for each indention. An indent load of 10 mN was selected to exclude a superposition of stress fields under plastic deformation between the indents. The load was applied in 5 s, a constant load was held for 2 s to complete the drift of the instrument, and the load was released in 5 s. The samples were anchored with a cross-sectional face using epoxy. By positioning the bulk side at the bottom of the apparatus and the oxide side at the top, we indented both in a vertical direction crossing the bulk/oxide interface and the lateral direction of the STSs. The same positions of the samples were observed using field emission SEM (FE-SEM, JEOL-7800F, JEOL) equipped with an EPMA analyzer (JXA-8500F, JEOL) for compositional analysis.

The *in situ* SEM tensile test was conducted using a microtest300 tensile jig module (Gatan, USA). For SEM (Inspect F, FEI Company, USA), the accelerating voltage was set to be less than 30 kV, in which the SEM resolution was less than 1 nm. The 10 mm gauge length of the half-dog-bone-shaped samples was stretched at a strain rate of 10⁻²/s with an equal force from approximately 50 to 150 N applied on the sample cross-sectional area.

3. RESULTS AND DISCUSSION

3.1. Microstructures of Oxide Scales. The cross-sectional view of SEM images and EPMA compositional distributions of Fe, Cr, O, and Ni presented in Figure 1 were analyzed to determine the microstructure in the oxide scales of STS4A, STS4B, STS4C, and STS3 (Table 1). The raw EPMA data with the compositional scale bar can be seen in Figures S1−S6. The visible nanoindentations in the SEM images in Figure 1 were used to determine the mechanical properties of
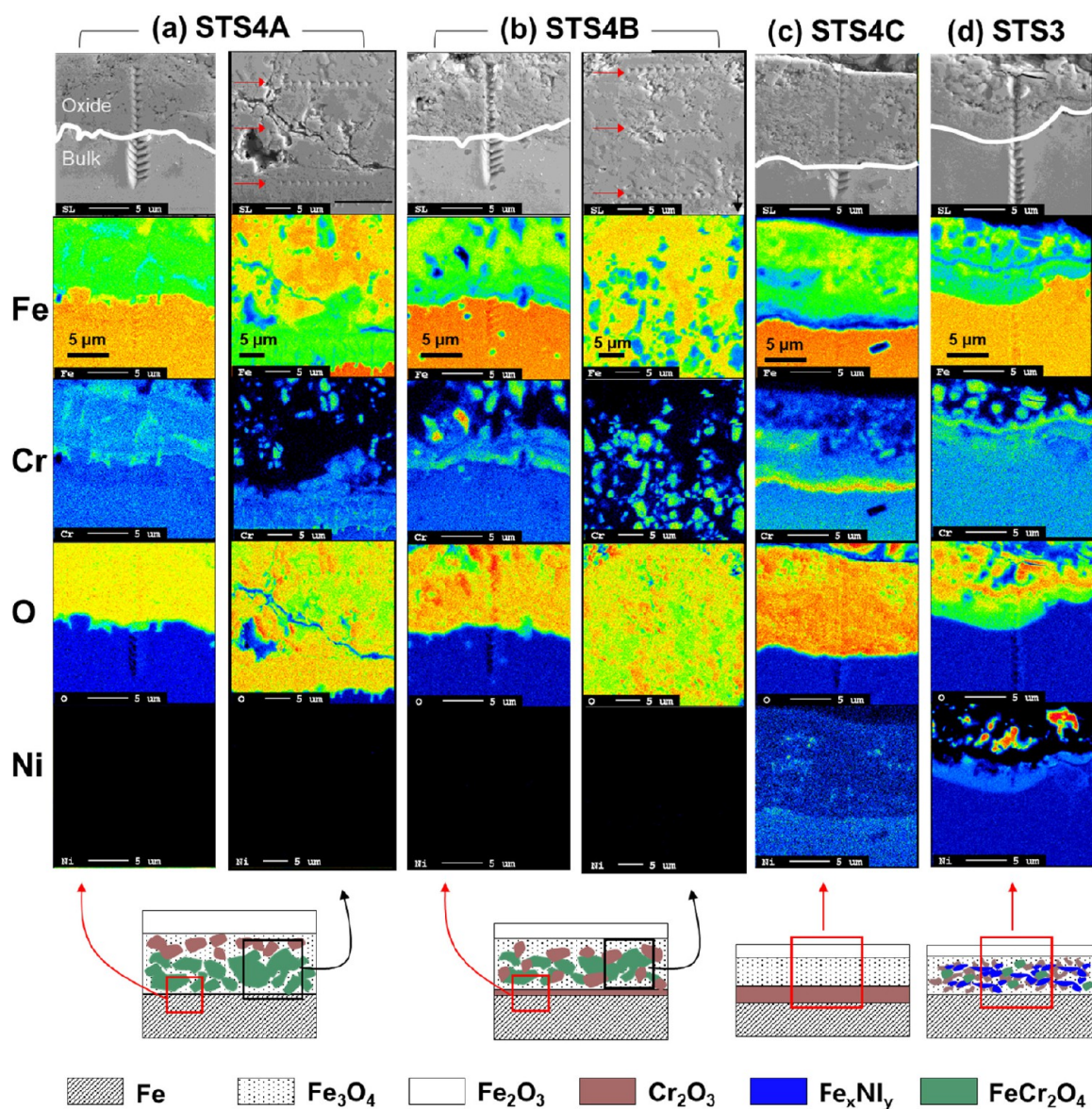
Figure 1. Cross-sectional SEM images and EPMA (Fe, Cr, O, and Ni) compositional distributions in the oxide scales of (a) STS4A, (b) STS4B, (c) STS4C, and (d) STS3. The oxide/bulk interfaces are marked with solid white lines, as indicated in the SEM images. Two different regions were analyzed in STS4A and STS4B due to their thick oxide scales, as shown in the schematic illustrations (bottom row of images) as red boxes around the bulk/oxide interfaces and black boxes far from the interfaces. The schematic images reveal the composition of the oxide scales on the basis of the EPMA analysis results and our previous work involving microstructural analyses.[13] The nanoindentation marks in the SEM images were used to analyze the variation in mechanical properties across the oxide/bulk interfaces and in the three equidistant regions (indicated by the red arrows) from the middle of the oxide scales, and the results are presented in Figure 6.

the oxide scales in relation to their composition and microstructure, as presented in Figures 2 and 6. The different colors and contrasts of the EPMA images depend on the atomic mass concentration (%) of each element. The positions of the bulk/oxide scale interfaces of the STSs were identified by comparing the O-deficient and Fe-rich areas of the EPMA elemental maps.

In ferritic sample STS4A (Table 1), with a low Cr content (Figure 1a), most of the evenly distributed Cr near the interface coexisted with the Fe-sufficient region, implying that the iron(II) chromite ($FeCr_2O_4$) inclusions were uniformly dispersed near the bulk/oxide interface.[15] However, above the $FeCr_2O_4$ inclusion-rich region on the STS4A oxide scale, Cr_2O_3 inclusions were surrounded by magnetite (Fe_3O_4), as Cr existed in discrete areas deficient in Fe. Similar to the case for STS4A, Cr_2O_3 inclusions also precipitated in the Fe_3O_4 matrix of STS4B, as shown in Figure 1b, but they coexisted with the $FeCr_2O_4$ inclusions above the very thin Cr_2O_3 layer above the bulk/oxide interface. In contrast, a thick Cr_2O_3 layer existed at the bulk/oxide interface in STS4C, followed sequentially by layers of Fe_3O_4 and hematite (Fe_2O_3) with very minute $FeCr_2O_4$ inclusions.

According to Figure 1a−c, with increasing Cr content from STS4A to STS4C, the number of $FeCr_2O_4$ inclusions decreased in the oxide scales and the thickness of the Cr_2O_3 layer at the bulk/oxide interface increased. In austenitic STS3 (Figure 1d), O-deficient and Ni-rich Fe_xNi_y intermetallic particles were embedded with Cr_2O_3 and $FeCr_2O_4$ inclusions in the Fe_3O_4 matrix, forming a composite-like structure.[15] These elemental analysis results agreed very well with previous
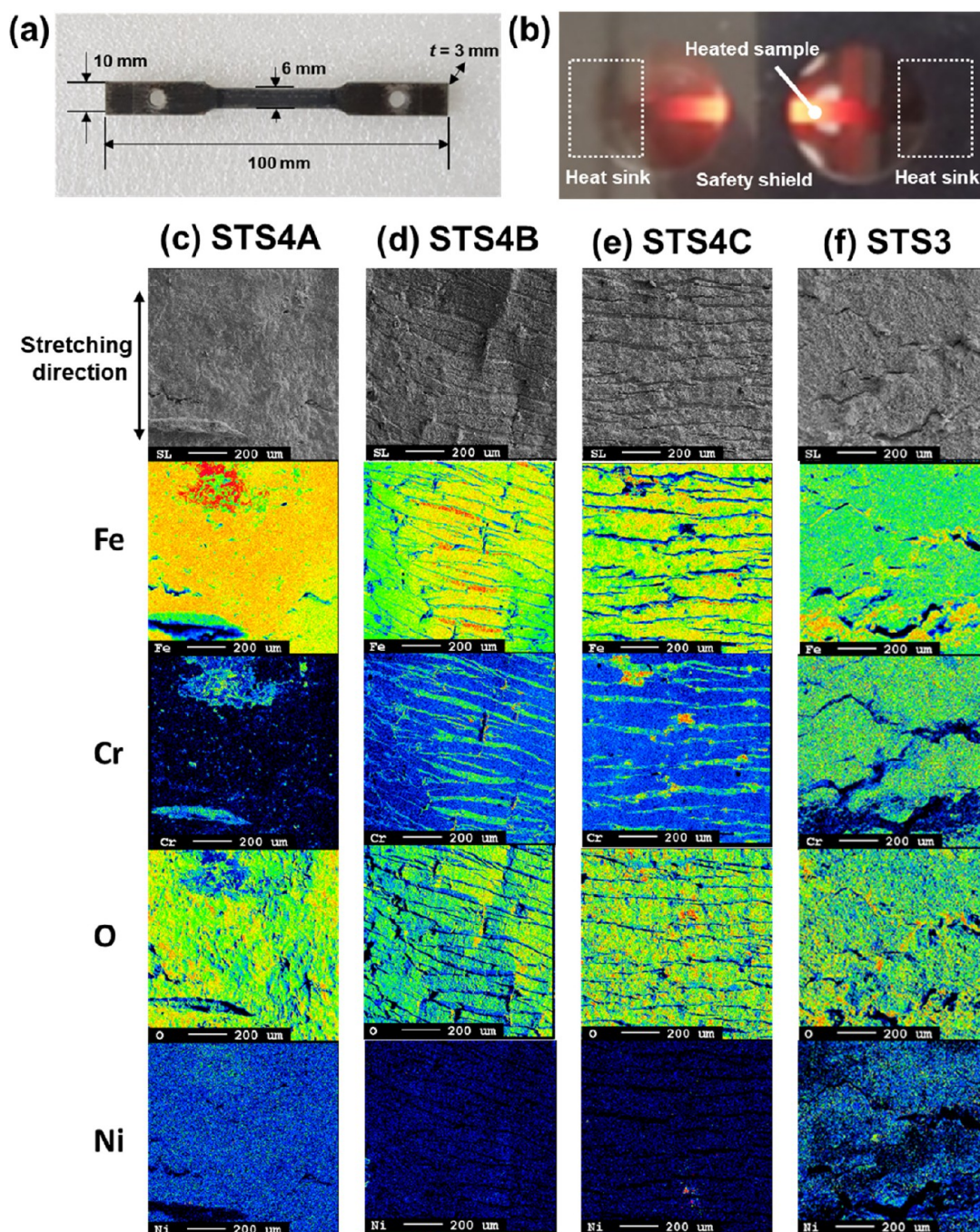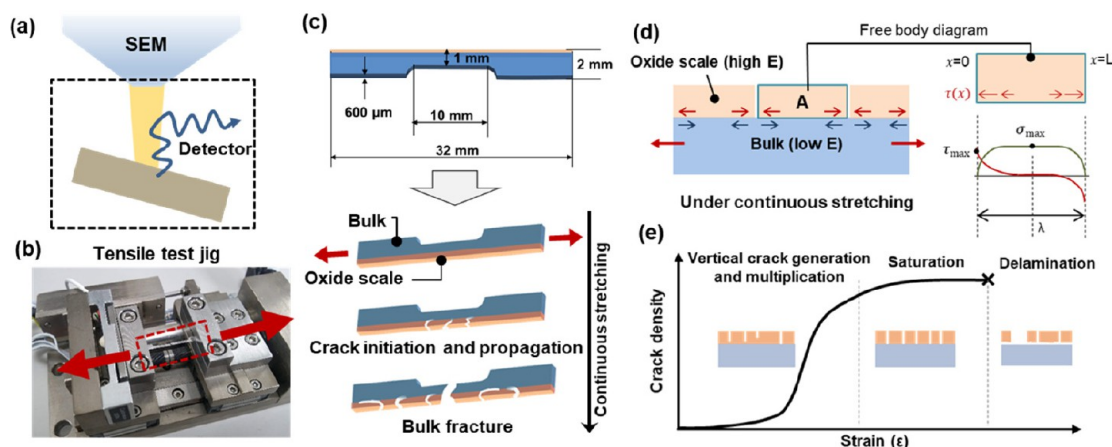
Figure 2. (a) Schematic descriptions of the Gleeble test specimen and (b) its real-time image under simultaneous heating and stretching conditions from outside of the safety shield. The sample was connected to heat sinks and glowed with 950 °C heating. Top view FE-SEM images and EPMA compositional distributions of (c) STS4A, (d) STS4B, (e) STS4C, and (f) STS3 after the Gleeble test under 20% strain.

studies,[15,24,25,27,28] showing that STSs with low and medium levels of Cr have oxide scales with composite-like distributions of Fe−Cr and Cr−oxide inclusions, while STSs containing high levels of Cr have oxide scales consisting of discrete and dense Fe− and Cr−oxide layers.[15]

3.2. Gleeble Test. Gleeble tests were performed with dog-bone-shaped specimens, as presented in Figure 2a. As shown in Figure 2b, the samples were anchored by a heat sink and glowed red by a direct resistance heating system. To understand the onset fracture mechanisms of STSs under hot rolling, the samples were stretched to only 20% strain at 950 °C, with a strain rate of 1 s^{-1} to avoid necking or delamination

of the oxide scale. With the elongated specimens, by using FE-SEM and EPMA, the morphology and the elemental distributions of the fractured top surfaces were investigated, respectively, as shown in Figure 2c−f. Each mass concentration (%) of Fe, Cr, O, and Ni was identified by the different degrees of contrast and colors in this experiment. The raw EPMA data with different compositional scale bars are presented in Figures S7−S10. Similarly to our previous study, STSs containing a low level of Cr (Figure 2c) and Ni (Figure 2f) were highly resistant to crack generation, while STSs containing a medium and high level of Cr showed frequent crack generation represented as a distinct O-deficient region (bulk exposure).

Figure 3. (a) Schematic illustration of the *in situ* SEM setup for the microtensile test of the STS samples and (b) photograph of the tensile test jig. (c) Schematic descriptions of the tensile specimen and its mechanical failure processes under continuous stretching. (d) Schematic illustration of the bulk/oxide interface and the free body diagram of the oxide scale segment represented by A. The graph below the free body diagram indicates the interfacial shear and normal stress distributions. (e) General crack propagation behavior in terms of crack density at the oxide scale, displaying three representative stages for delamination or descaling failure.

Beyond investigating the *ex situ* top-view crack generation, we need to determine the dynamic mechanisms of crack initiation and how cracks propagate through the thickness of the oxide scale with regard to the distribution of microstructural compositions and their mechanical properties.

3.3. Failure Modes of Oxide Scales under Tensile Loading. The *in situ* SEM tensile tests were performed on a tensile test jig, as depicted in Figure 3a. Cracking started from the surface of the brittle oxide scales and then progressed through the thickness of the scales. Cross-sectional crack initiation and propagation observations were possible only in the half-dog-bone-shaped specimens (Figure 3c). *In situ* tensile tests were conducted until the number of cracks was saturated, followed by bulk fracture of the STSs.

During tensile loading to a two-layered structure with different mechanical properties—particularly brittle/ductile properties—crack initiation and propagation behaviors can be determined by the superiority between the interfacial strength and vertical fracture strength. As shown in Figure 3d, due to the higher modulus of the oxide scale in comparison to that of the bulk, interfacial shear stress is applied to both ends of the oxide scale. Here, the interfacial shear stress ($\tau(x)$) has distributions along the x axis (from $x = 0$ to $x = L$), and the maximum interfacial shear stress (τ_{max}) is applied at both ends of the fractured oxide segment. At the same time, by a force balance within the oxide scale, the applied $\tau(x)$ value can be transferred as the normal stress $\sigma(x)$ value at the center of the oxide fragments by eq 1

$$\sigma(x) = 1/t \int \tau(x) \, dx \qquad (1)$$

where t represents the thickness of the oxide scale, assuming that the in-plane normal stress is uniformly distributed throughout the cross-sectional area (orthogonal to the plane of the paper or diagram) of the samples.[20,29]

$\sigma(x)$ is also a function of position x, which reaches a maximum value (σ_{max}) within the middle plateau region of the fractured oxide segment. Therefore, the uniaxially applied tensile load is transferred to $\tau(x)$ at the interface between the oxide scale and the bulk, particularly at both ends of the oxide scale, and then, it is also transferred to $\sigma(x)$ in the middle of

the oxide scale. Here, a vertical crack is first generated in the middle of the oxide scale when the transferred σ_{max} is larger than the critical stress (σ_c) for the vertical fracture of the oxide scale ($\sigma_c = E_{ox}\varepsilon_{on}$, where E_{ox} is the elastic modulus of the oxide and ε_{on} is the onset strain of the fracture). With progressing crack generation, the transferred σ_{max} decreases due to the reduced $\tau(x)$ as the overall lengths of segments decrease, resulting in no additional vertical crack generation and saturation, as schematically illustrated in Figure 3e.

With the length of the oxide scale segments determining the width of the intercrack spacing (λ), Chen[20] developed the relationship between the smallest characteristic intercrack spacing (λ_c) and τ_{max} using eq 2.[20] Here, with the smallest crack segment, $\sigma_{max} = E_{ox}\varepsilon_{on}$ exists as a point rather than a plateau region.

$$\tau_{max} = 4t\sigma_{max}/((4 + \pi)\lambda_c) = 4tE_{ox}\varepsilon_{on}/(4 + \pi)\lambda_c \qquad (2)$$

After the vertical crack initiation and multiplication of the cracks, the formation of vertical cracks reaches saturation when the crack density is high enough to be limited by λ_c.[20,22,30] Finally, eq 2 provides an interpretation tool for the interfacial strength between two layers having different mechanical properties, where the variation in crack density ($1/\lambda_c$) coupled with the fracture strength ($E_{ox}\varepsilon_{on}$) is reflected as τ_{max}. For example, the smaller the τ_{max} between the two layers, the higher the possibility of crack propagation along the bulk/oxide interface rather than vertical crack generation.[30]

The cross-sectional crack patterns in the oxide scales of STS4A, STS4B, STS4C, and STS3 at strains of 2%, 4%, 6%, 8%, and 10% are shown in Figure 4. At a strain of 2%, all of the STS oxide scales had cracks that were generated from their surfaces through their thickness. Varying crack patterns then developed in the oxide scales as the strain increased to 10%, depending on the type of STS. While vertical crack generation was dominant in STS4A, vertical and lateral cracks (parallel to the bulk/oxide scale interface) were generated in STS4B and STS3. Furthermore, the vertical crack tips arriving at the bulk/oxide scale interfaces in STS4B and STS3 did not propagate further across the interface, as if the tips were pinned at the interface. In contrast, the initially generated vertical cracks in the STS4C oxide scale propagated along the bulk/oxide
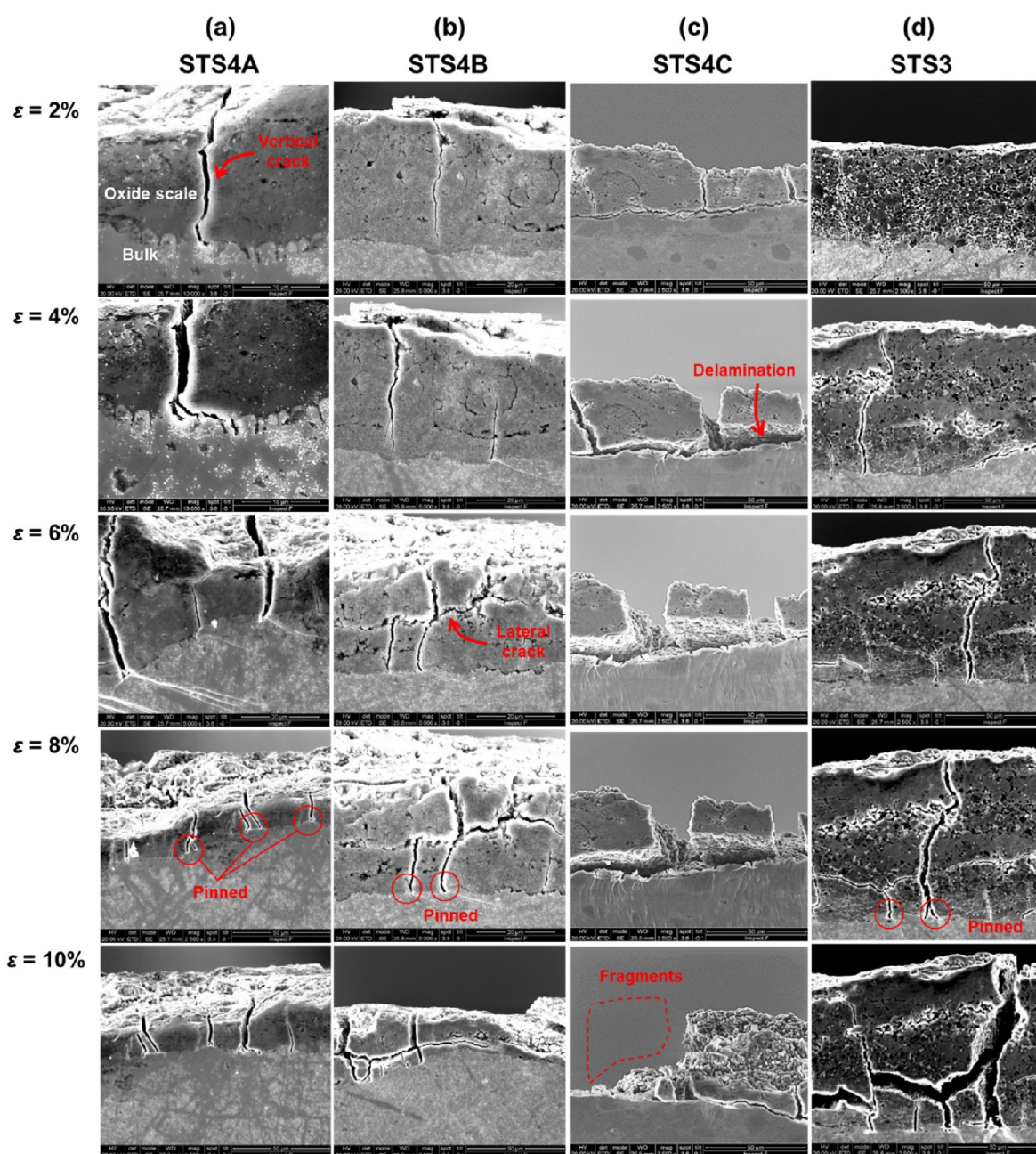
Figure 4. *In situ* SEM images of the crack patterns and propagation in the oxide scales of (a) STS4A, (b) STS4B, (c) STS4C, and (d) STS3 at strains (ε) of 2%, 4%, 6%, 8%, and 10% during a tensile test analysis.

interface as the strain reached 4%. These interfacial cracks then resulted in an unexpected descaling of the oxide scale from the bulk of STS4C.

On the basis of the relationship between the interfacial strength and crack density, provided as eq 2, the variation in crack density with the four different STSs is analyzed as shown in Figure 5. The long-range crack patterns in each oxide scale of the STSs at strains of 4% and 10% shown in Figure 5a−d were determined by SEM micrographs. The vertical cracks that initiated at a strain of 2% continued to propagate through the thickness of the oxide scales or were followed by the generation of lateral cracks along with the interfaces of the oxide inclusions. The intercrack spacing and normalized density of vertical cracks within the oxide scale length of 300 μm at strains of 2%, 4%, 6%, 8%, and 10% were measured for

each sample, as shown in Figures 5e,f, respectively. Because the crack spacing is inversely proportional to the crack density, the lower vertical crack spacing in STS4A, STS4B, and STS3 than in STS4C indicated that more vertical oxide scale cracks were generated in STS4A, STS4B, and STS3.

In Figure 5e, the intercrack spacing in the oxide scales became saturated when the strain was 8%, 6%, and 4% for STS4A, STS4B, and STS4C, respectively. STS3 showed a continuous decrease until 10% strain. With the lowest strain of STS4C for the onset of vertical crack saturation, the highest saturated intercrack spacing value indicated that crack propagation through the bulk/oxide interface overcame the additional formation of vertical cracks to relax the strain energy applied in STS4C in comparison with the other three types of STSs in this work. As illustrated in Figure 5f, the normalized
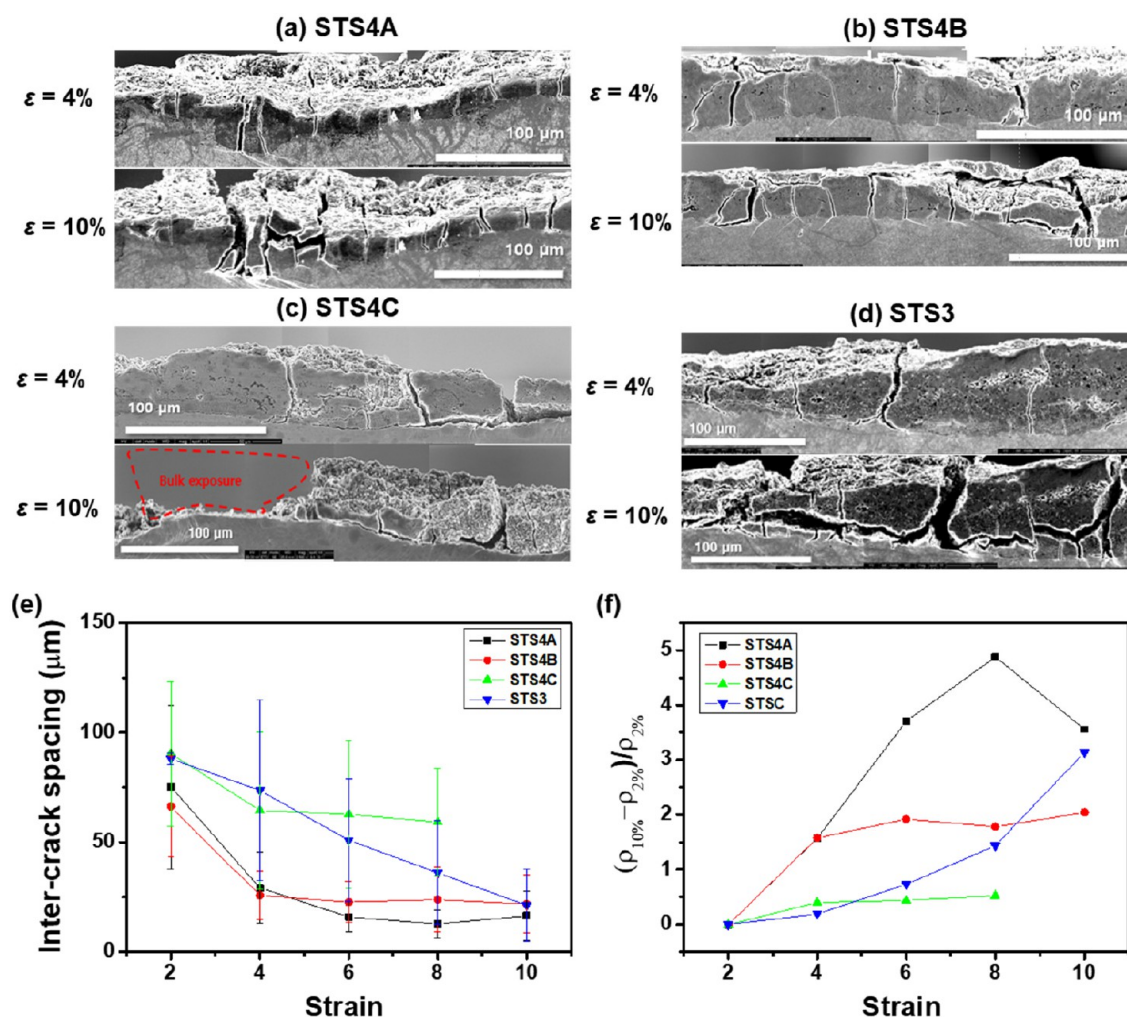
Figure 5. SEM images of the long-range fracture patterns in the oxide scales of (a) STS4A, (b) STS4B, (c) STS4C, and (d) STS3 at strains of 2% and 10%. (e) Intercrack spacing (vertical cracks) and (f) normalized vertical crack density of each sample as a function of strain.

vertical crack density can be obtained from the difference between the crack densities $(1/(\text{mean value of the intercrack spacing}))$ at strains of 10% $(\rho_{10\%})$ and 2% $(\rho_{2\%})$, in which STS4A exhibited the highest increase in vertical crack density and STS4C exhibited the lowest increase in vertical crack density and the lowest strain when the vertical crack density was saturated. Vertical cracks in the oxide scales of STS4A, STS4B, and STS3 continuously increased, even beyond a strain of 4%.

The applied strain energy relaxes through bond breakage inside the oxide scales after new fracture site formation. The strain energy relaxation in the STS4B and STS3 oxide scales evolved by either lateral or vertical direction debonding following the initial formation of vertical cracks at the oxide scale surface due to the distribution of Cr_2O_3 inclusions with weak cohesive energy. Therefore, the lower normalized vertical crack density in the STS4B and STS3 oxide scales in comparison to that in the STS4A oxide scale was ascribed to the relaxation of elastic strain energy through the additional intermediate lateral debonding.

3.4. Mechanical Properties of Oxide Scales. To interpret the interfacial strength of the four STSs in combination with the crack density results obtained in Figure 5, we determined the mechanical properties of the oxide scales with varying compositions and microstructures by a nano-

indentation method,[31] as illustrated in Figure S11. Nano-indentations spaced at 1 and 2 μm were observed vertically across the bulk/oxide scale interfaces and laterally parallel to the interfaces, respectively, as in Figure 1. From the cross-sectional SEM images, we confirmed that the indents of oxide scales are independent of each other from the stress field (Figures S1−S6). Three parallel and equidistant lines of lateral nanoindentations were used to determine the mechanical property variations in the oxide scales at the different locations. The theory for the derivation of the modulus (E) and hardness (H) from the nanoindentation test results is presented in section S11 of the Supporting Information.

The distributions of E and H in the oxide scales are plotted in Figure 6. The oxide scale on ferritic STS4A had uniform distributions of E and H at approximately 125 and 8 GPa, respectively, near the bulk/oxide scale interface; this was caused by the evenly distributed $FeCr_2O_4$ inclusions embedded in the Fe_3O_4 matrix, according to the vertical nanoindentation results presented in Figure 6a. However, both the average E and H values of the oxide scale of STS4A decreased from its bottom region (136 and 9 GPa, respectively) toward its top region (95 and 5 GPa, respectively). Hence, the top area containing the Cr_2O_3 inclusions embedded in the Fe_3O_4 matrix has both low E and low H.
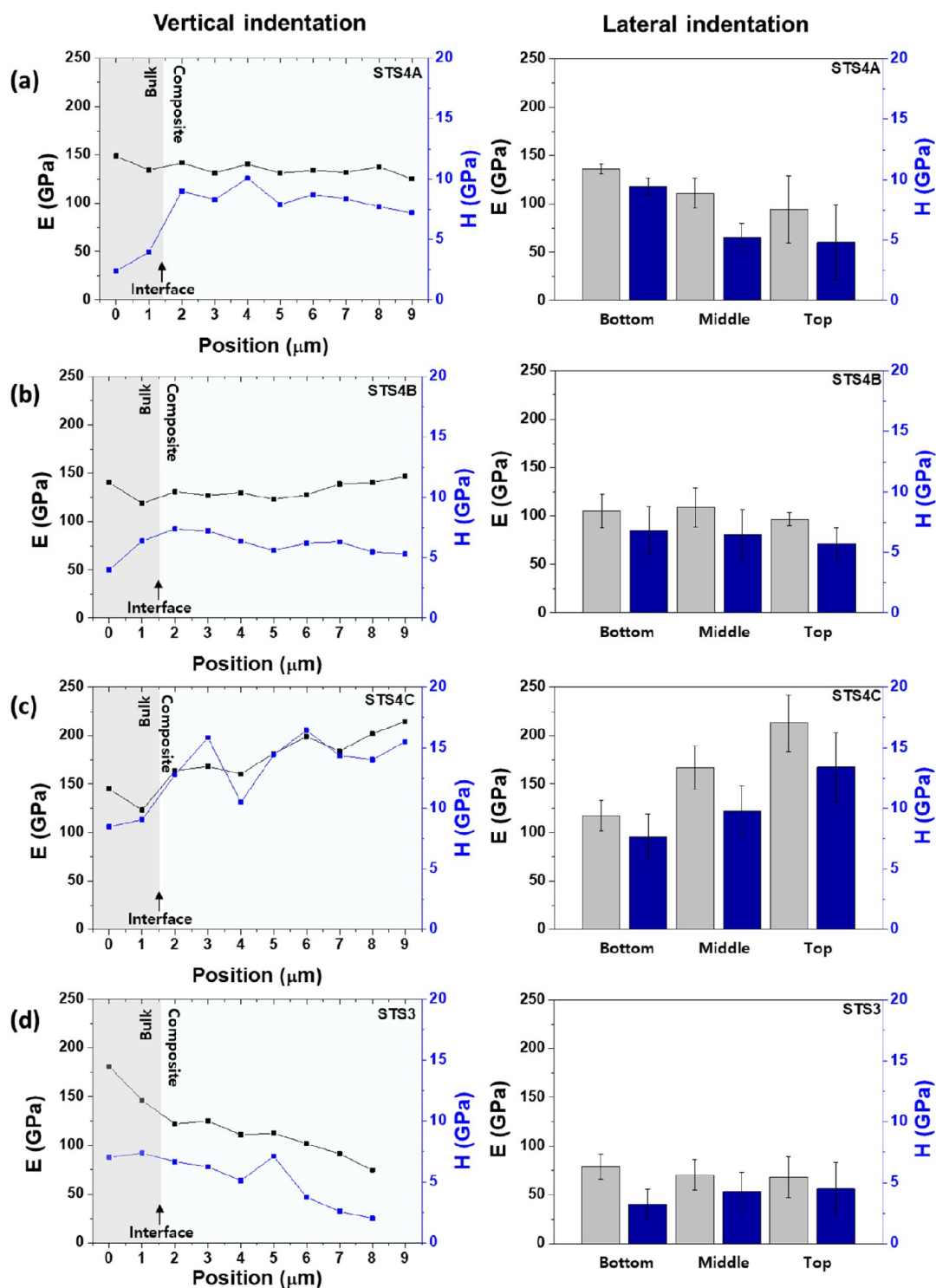
Figure 6. Elastic modulus (*E*) and hardness (*H*) obtained from vertical (left column graphs) and lateral (right column graphs) nanoindentations of the oxide scales of (a) STS4A, (b) STS4B, (c) STS4C, and (d) STS3. The bottom, middle, and top locations in the lateral indentation graphs were equidistant regions from the center of the oxide scales. The bottom, middle, and top sites were near the bulk/oxide interface, at the center of the oxide scales, and near the surface of the oxide scales, respectively.

In Figure 6b, the oxide scale on ferritic STS4B near the bulk/oxide scale interface had *E* and *H* values similar to those of STS4A at approximately 140 and 6 GPa, respectively. On the other hand, both *E* and *H* across the STS4B oxide scale thickness were almost constant at approximately 110 and 7 GPa, respectively, close to values obtained from the top region of the STS4A oxide scale with Cr_2O_3 inclusions. These

measurement results imply that the locations of the Cr_2O_3 inclusions were distributed throughout the oxide scale in STS4B, while they were concentrated in the top region of the STS4A oxide scale.

In Figure 6c, STS4C—with the highest Cr content—had a thick Cr_2O_3 layer above the bulk/oxide interface, with *E* and *H* values of approximately 120 and 8 GPa, respectively, being

similar to regions in STS4A and STS4B containing Fe_3O_4 layers with Cr_2O_3 inclusions. In contrast, the Fe_3O_4 layer on top of the Cr_2O_3 layer on the STS4C oxide scale had higher E and H values of approximately 210 and 13 GPa, respectively. Because Cr has a high oxidation potential,[24,32] the Cr_2O_3 layer forms easily at the bulk/oxide scale interfaces, resulting in the slow formation of a dense Fe oxide on top of Cr_2O_3. Only Fe can diffuse outward from the reactive zone of the concentrated Cr_2O_3 layer because Fe has a higher diffusivity in comparison to Cr and Ni.[24,25,32,33] Further oxidation leads to the formation of a dense Cr_2O_3 layer, in which the abundant Fe continually diffuses out from the bulk, forming a dense layer of Fe_3O_4 and Fe_2O_3.[24]

The oxide scale of STS3 near the bulk/oxide interface had E and H values of approximately 80 and 2 GPa, respectively, lower than those of the bulk STS (E and H of approximately 125 and 7 GPa, respectively), as shown in Figure 6d. In comparison to STS4B with an equivalent Cr content (Figure 6b), STS3 has an oxide layer with a composite structure containing the O-deficient intermetallic compound Fe_xNi_y, leading to low E and H values of approximately 70 and 4 GPa, respectively. Hence, dense oxides without inclusions in their structures have high E and H values, whereas mixed composite oxides and Cr_2O_3 components have low E and H values.

3.5. Failure Models of the Oxide Scales in STSs with Different Cr Contents. On the basis of the results of saturated crack density and elastic modulus discussed in sections 3.3 and 3.4, respectively, τ_{max} values of the four STSs were calculated using eq 2, and the values are presented in Table 2. E_{ave} is the average elastic modulus calculated from the

Table 2. Calculated τ_{max} Values of the Four Types of STSs using eq 2[a]

sample	t (μm)	λ_c (μm)	ε_{on} (%)	ε_{sat} (%)	E_{ave} (GPa)	τ_{max} (GPa)
STS4A	24.7	16.1	2	8	123.74	2.13
STS4B	30.1	15.1	2	6	107.09	2.39
STS4C	37.9	97.9	2	4	165.78	0.72
STS3	48.5	29.7	2	>10	72.47	1.33

[a]h is the thickness of the oxide scale. λ_c is the saturated vertical crack spacing in Figure 5e. ε_{on} and ε_{sat} are the vertical crack generation onset strain and the saturation strain, respectively.

lateral nanoindentation results. For the STS4 series, both STS4A and STS4B exhibited similarly high τ_{max} values of 2.13 and 2.39, respectively, whereas the lowest τ_{max} of 0.72 was observed in STS4C (Table 2). The high τ_{max} value explains the substantial crack pinning effect at the bulk/oxide scale interface in STS4A and STS4B, as shown in Figure 4a,b, respectively. However, whereas only vertical cracks developed at the oxide scale of STS4A, the oxide scale of STS4B exhibited both vertical and lateral crack propagation. The different crack patterns between the oxide scales of STS4A and STS4B—despite the similar high τ_{max} values—can be explained by their distinct E distributions in the through-thickness direction of the oxide scale.

How different crack patterns were correlated with the E distributions throughout the thickness of the oxide scale can be understood through fracture toughness (K_c).[34,35] On the assumption that the oxide scales are isotropic and linear elastic (following linear elastic fracture mechanics), their K_c value is then associated with the critical stress for crack propagation (σ_c) and crack length (a)

$$K_c = (2E\gamma_s)^{1/2} = Y\sigma_c(\pi a)^{1/2} \tag{3}$$

where γ_s is the specific surface energy and Y is the dimensionless parameter that takes into account the crack condition and specimen shape.[36,37] Accordingly, the fracture propagates through the oxide scales along the path with the lowest E value. In STS4A, E increased from the surface of the oxide scale toward the bulk/oxide scale interface (Figure 4a). Hence, the easiest method to release the stored strain energy at the STS4A oxide scale was to fracture new vertical sites at the oxide scale surface and then propagate toward the bulk/oxide scale interface. In contrast, E did not vary significantly throughout the oxide scale of STS4B, as shown in Figure 4b. Therefore, there was no preferred crack propagation path in the STS4B oxide scale after formation of the initial vertical crack. The stored strain energy was randomly released within the oxide scale of STS4B, resulting in the evolution of both vertical and lateral crack patterns, as schematically illustrated in Figure 7.

On the other hand, the significantly low τ_{max} value of STS4C implies the lowest interfacial adhesion energy between the oxide and bulk. Accordingly, the stored strain energy was predominantly released through delamination and descaling. As depicted in Figures 4a,c, in comparison to that of STS4A, the oxide scale of STS4C has a reverse E distribution along its thickness, causing vertical crack generation to become the most challenging approach for releasing the stored strain energy in the oxide scale of STS4C. Therefore, a positive coupling between the low interfacial adhesion energy and high fracture toughness on top of the oxide scale induces delamination of the oxide scale and exposure of the bulk STS in STS4C, which eventually results in sticking failure (Figure 7).

An intermediate τ_{max} value of 1.33 of the STS3 oxide scale (among all four samples in this work) was in contrast to the observed vertical crack pinning at the bulk/oxide scale interface and the random vertical and lateral crack patterns shown in Figure 4 without oxide descaling, similar to the case fir STS4C. In contrast, the oxide scale of STS3 showed the same crack patterns as that of the oxide scale of STS4B, with a τ_{max} value of 2.39. The distinctive feature of STS3 involving the uniformly dispersed Fe_xNi_y intermetallic particles mixed with other Fe- and Cr-based oxides resulted in an underestimation of its E value and, in turn, its τ_{max} value. As in the case of STS4B, the almost uniform distribution of E in the oxide scale of STS3 allowed random crack propagation through either the lateral or vertical direction (Figure 7).

4. CONCLUSION

This paper describes the failure mechanisms for the oxide scales of four differently alloyed STSs on the basis of the τ_{max} and E distributions throughout the oxide scales. From the lowest (11 wt %) to highest (21 wt %) Cr content STSs, the oxide scales evolved from having a composite-like structure with Cr_2O_3 and $FeCr_2O_4$ inclusions to having a dense layer of Cr_2O_3 near the bulk/oxide interface. The layered structured Fe−oxide components of the oxide scale formed on the top of the Cr_2O_3 layer in STS with the highest Cr content. A Gleeble test and *ex situ* analysis of the exposed fractured surfaces on the oxide scales were validated using *in situ* SEM tensile tests coupled with nanoindentation. The different vertical crack densities and crack propagation paths in the four STSs originated from the microstructural composition and mechanical properties within the oxide scales, which determines the
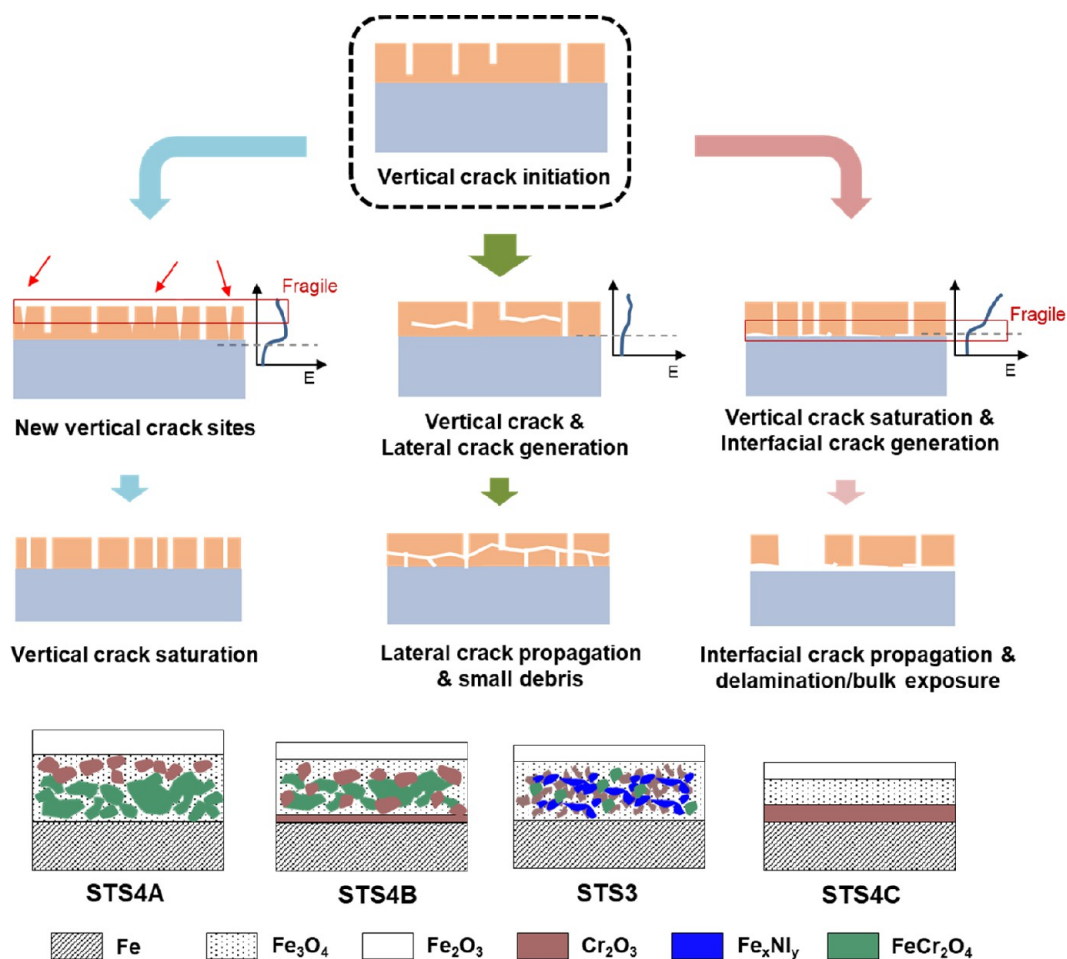
Figure 7. Schematic illustration of three failure models involving the progress of oxide scale crack initiation, propagation, and interfacial delamination of the four types of STSs.

superiority between the development of new vertical cracks from the top region and interfacial delamination from the oxide/bulk region.

After the initial vertical crack generation, delamination was observed in the bulk/oxide interface of the highest-Cr-content STS4C due to its bottom-layer Cr_2O_3 with low fracture toughness. In contrast, additional vertical cracks were generated on the top of the oxide scales in the lowest-Cr-content STS4A with a gradual increasing E value from its top surface toward its interface. Furthermore, vertical and lateral propagations were simultaneously observed in the STS oxide scales with intermediate Cr contents (STS4B and STS3), exhibiting a distribution of Cr_2O_3 inclusions and uniform E distributions throughout the oxide scales. Finally, we concluded that the distribution of Cr_2O_3 inclusions in the oxide scales determined the crack propagation path because the inclusions exhibited both the lowest E value and fracture toughness in comparison with the other microstructural components of the oxide scales. Hence, this study suggests that the formation of Cr_2O_3 due to the Cr content in STSs should be finely tuned to avoid sticking failure by preventing crack propagation through the bulk/oxide scale interface.

ASSOCIATED CONTENT

Supporting Information

The Supporting Information is available free of charge at https://pubs.acs.org/doi/10.1021/acsomega.2c01267.

Cross-sectional view FE-SEM images and EPMA compositional distributions around the bulk/oxide interfaces in all of the samples analyzed in this work and an nanoindentation analysis (PDF)

AUTHOR INFORMATION

Corresponding Author

Jin-Woo Park − *Department of Materials Science and Engineering, Yonsei University, Seoul 03722, Republic of Korea*; orcid.org/0000-0003-0965-373X; Phone: +82-221235834; Email: jwpark09@yonsei.ac.kr; Fax: +82-221235834

Authors

Soyeon Lee − *Department of Materials Science and Engineering, Yonsei University, Seoul 03722, Republic of Korea*

Seung-Rok Kim − *Department of Materials Science and Engineering, Yonsei University, Seoul 03722, Republic of Korea*

Ross E. Triambulo − *Department of Materials Science and Engineering, Yonsei University, Seoul 03722, Republic of Korea*

Chang-Jin Lim − *Department of Materials Science and Engineering, Yonsei University, Seoul 03722, Republic of Korea*

Han-Jin Kim − *Center for Energy Materials Research, Korea Institute of Science and Technology, Seoul 02792, Republic of Korea*

Jin-Yoo Suh − *Center for Energy Materials Research, Korea Institute of Science and Technology, Seoul 02792, Republic of Korea*

Hyung-Gu Kang − *Stainless Steel Research Group, Technical Research Laboratory, POSCO, Pohang 37859, Republic of Korea*

Complete contact information is available at:
https://pubs.acs.org/10.1021/acsomega.2c01267

Author Contributions

The manuscript was written through contributions of all authors. All authors have given approval to the final version of the manuscript.

Author Contributions

‖S.L. and S.-R.K. contributed equally.

Author Contributions

⊥Asen Company, Seoul, Korea.

Notes

The authors declare no competing financial interest.

■ REFERENCES

(1) Lula, R. A. *Stainless steel*; American Society for Metals: Russell Township, 1985.

(2) Lo, K. H.; Shek, C. H.; Lai, J. K. L. Recent developments in stainless steels. *Mater. Sci. Eng. R-Rep.* **2009**, *65* (4), 39−104.

(3) Davis, J. R. *Stainless steels*; ASM international: 1994.

(4) Son, C.-Y.; Kim, C. K.; Ha, D. J.; Lee, S.; Lee, J. S.; Kim, K. T.; Lee, Y. D. Mechanisms of sticking phenomenon occurring during hot rolling of two ferritic stainless steels. *Metall. Mater. Trans. A* **2007**, *38* (11), 2776.

(5) Park, S. H. C.; Sato, Y. S.; Kokawa, H.; Okamoto, K.; Hirano, S.; Inagaki, M. Corrosion resistance of friction stir welded 304 stainless steel. *Scr. Mater.* **2004**, *51* (2), 101−105.

(6) Xiong, Y.; Yue, Y.; Lu, Y.; He, T.; Fan, M.; Ren, F.; Cao, W. Cryorolling impacts on microstructure and mechanical properties of AISI 316 LN austenitic stainless steel. *Mater. Sci. Eng., A* **2018**, *709*, 270−276.

(7) Zhang, C.; Liu, Z. Y.; Xu, Y.; Wang, G. D. The sticking behavior of an ultra purified ferritic stainless steel during hot strip rolling. *J. Mater. Process. Technol.* **2012**, *212* (11), 2183−2192.

(8) Ha, D. J.; Sung, H. K.; Lee, S.; Lee, J. S.; Lee, Y. D. Analysis and prevention of sticking occurring during hot rolling of ferritic stainless steel. *Mater. Sci. Eng., A* **2009**, *507* (1−2), 66−73.

(9) Ha, D. J.; Lee, J. S.; Kim, N. J.; Lee, S. Effects of Alloying Elements on High-Temperature Oxidation and Sticking Occurring During Hot Rolling of Modified Ferritic STS430J1L Stainless Steels. *Metall. Mater. Trans. A* **2012**, *43A* (1), 74−86.

(10) Hao, L.; Jiang, Z. Y.; Cheng, X. W.; Zhao, J. W.; Wei, D. B.; Jiang, L. Z.; Luo, S. Z.; Luo, M.; Ma, L. Effect of Extreme Pressure Additives on the Deformation Behavior of Oxide Scale during the Hot Rolling of Ferritic Stainless Steel Strips. *Tribol. Trans.* **2015**, *58* (5), 947−954.

(11) Hao, L.; Jiang, Z. Y.; Wei, D. B.; Gong, D. Y.; Cheng, X. W.; Zhao, J. W.; Luo, S. Z.; Jiang, L. Z. Experimental and Numerical Study on the Effect of ZDDP Films on Sticking During Hot Rolling of Ferritic Stainless Steel Strip. *Metall. Mater. Trans. A* **2016**, *47A* (10), 5195−5202.

(12) Zhou, C. H.; Pan, R. Y.; Ma, H. T.; Zhang, H.; Guan, X. G.; Mao, N. N.; Sun, F. J. Oxidation Kinetics Researches under the Condition of Compressive Loading. *IOP Conf. Ser.: Mater. Sci. Eng.* **2018**, *389*, 012017.

(13) Noh, W.; Lee, J.-M.; Kim, D.-J.; Song, J.-H.; Lee, M.-G. Effects of the residual stress, interfacial roughness and scale thickness on the spallation of oxide scale grown on hot rolled steel sheet. *Mater. Sci. Eng., A* **2019**, *739*, 301−316.

(14) Dubois, A.; Luc, E.; Dubar, M.; Dubar, L.; Thibaut, C.; Damasse, J.-M. Initiation of Sticking during Hot Rolling of Stainless Steel Plate. *Procedia Eng.* **2014**, *81*, 1958−1963.

(15) Kim, S.-R.; Lee, S.; Kang, H.-G.; Park, J.-W. Oxide scale on stainless steels and its effect on sticking during hot-rolling. *Corros. Sci.* **2020**, *164*, 108357.

(16) Zhang, C.; Larionov, K. V.; Firestein, K. L.; Fernando, J. F. S.; Lewis, C.-E.; Sorokin, P. B.; Golberg, D. V. Optomechanical Properties of MoSe2 Nanosheets as Revealed by In Situ Transmission Electron Microscopy. *Nano Lett.* **2022**, *22* (2), 673−679.

(17) Pascal, C.; Braccini, M.; Parry, V.; Fedorova, E.; Mantel, M.; Oquab, D.; Monceau, D. Relation between microstructure induced by oxidation and room-temperature mechanical properties of the thermally grown oxide scales on austenitic stainless steels. *Mater. Charact.* **2017**, *127*, 161−170.

(18) Chandra-Ambhorn, S.; Roussel-Dherbey, F.; Toscan, F.; Wouters, Y.; Galerie, A.; Dupeux, M. Determination of mechanical adhesion energy of thermal oxide scales on AISI 430Ti alloy using tensile test. *Mater. Sci. Technol.* **2007**, *23* (4), 497−501.

(19) Liang, J.; Wang, Z.; Xie, H.; Li, X. In situ scanning electron microscopy-based high-temperature deformation measurement of nickel-based single crystal superalloy up to 800 °C. *Opt Lasers Eng.* **2018**, *108*, 1−14.

(20) Chen, B. F.; Hwang, J.; Chen, I. F.; Yu, G. P.; Huang, J. H. A tensile-film-cracking model for evaluating interfacial shear strength of elastic film on ductile substrate. *Surf. Coat. Technol.* **2000**, *126* (2), 91−95.

(21) Galerie, A.; Toscan, F.; Dupeux, M.; Mougin, J.; Lucazeau, G.; Valot, C.; Huntz, A.-M.; Antoni, L. Stress and adhesion of chromia-rich scales on ferritic stainless steels in relation with spallation. *Mater. Res. (Sao Carlos, Braz.)* **2004**, *7*, 81−88.

(22) Nagl, M. M.; Evans, W. T.; Hall, D. J.; Saunders, S. R. J. An in situ investigation of the tensile failure of oxide scales. *Oxid. Met.* **1994**, *42* (5−6), 431−449.

(23) Chandra-ambhorn, S.; Wouters, Y.; Dupeux, M.; Galerie, A.; Antoni, L.; Toscan, F. In *Adhesion behaviour of thermal oxide scales grown on ferritic stainless steels proposed as interconnects in SOFCs*. Proc. - Electrochem. Soc. **2005**, *2005-07*, 1816−1821.

(24) Zeng, Z.; Natesan, K.; Cai, Z.; Gosztola, D.; Cook, R.; Hiller, J. Effect of Element Diffusion Through Metallic Networks During Oxidation of Type 321 Stainless Steel. *J. Mater. Eng. Perform.* **2014**, *23* (4), 1247−1262.

(25) Col, A.; Parry, V.; Pascal, C. Oxidation of a Fe−18Cr−8Ni austenitic stainless steel at 850°C in O2: Microstructure evolution during breakaway oxidation. *Corros. Sci.* **2017**, *114*, 17−27.

(26) Oliver, W. C.; Pharr, G. M. Measurement of hardness and elastic modulus by instrumented indentation: Advances in understanding and refinements to methodology. *J. Mater. Res.* **2004**, *19* (1), 3−20.

(27) Cheng, X.; Jiang, Z.; Wei, D.; Hao, L.; Zhao, J.; Jiang, L. Oxide scale characterization of ferritic stainless steel and its deformation and friction in hot rolling. *Tribol. Int.* **2015**, *84*, 61−70.

(28) Yang, C.-W.; Kim, J.-H.; Triambulo, R. E.; Kang, Y.-H.; Lee, J.-S.; Park, J.-W. The mechanical property of the oxide scale on Fe−Cr alloy steels. *J. Alloys Compd.* **2013**, *549*, 6−10.

(29) Agrawal, D. C.; Raj, R. Measurement of the ultimate shear strength of a metal-ceramic interface. *Acta Metall.* **1989**, *37* (4), 1265−1270.

(30) Bouaziz, H.; Brinza, O.; Haddar, N.; Gasperini, M.; Feki, M. In-situ SEM study of crack initiation, propagation and interfacial

debonding of Ni-P coating during tensile tests: Heat treatment effect. *Mater. Charact.* **2017**, *123*, 106−114.

(31) Rosenkranz, A.; Reinert, L.; Gachot, C.; Aboufadl, H.; Grandthyll, S.; Jacobs, K.; Müller, F.; Mücklich, F. Oxide Formation, Morphology, and Nanohardness of Laser-Patterned Steel Surfaces. *Adv. Eng. Mater.* **2015**, *17* (8), 1234−1242.

(32) Diawara, B.; Beh, Y.-A.; Marcus, P. Nucleation and Growth of Oxide Layers on Stainless Steels (FeCr) Using a Virtual Oxide Layer Model. *J. Phys. Chem. C* **2010**, *114* (45), 19299−19307.

(33) Sánchez, L.; Hierro, M. P.; Pérez, F. J. Effect of Chromium Content on the Oxidation Behaviour of Ferritic Steels for Applications in Steam Atmospheres at High Temperatures. *Oxid. Met.* **2009**, *71* (3), 173.

(34) Weikert, T.; Wartzack, S.; Baloglu, M. V.; Willner, K.; Gabel, S.; Merle, B.; Pineda, F.; Walczak, M.; Marian, M.; Rosenkranz, A.; Tremmel, S. Evaluation of the surface fatigue behavior of amorphous carbon coatings through cyclic nanoindentation. *Surf. Coat. Technol.* **2021**, *407*, 126769.

(35) Zambrano, D. F.; Villarroel, R.; Espinoza-González, R.; Carvajal, N.; Rosenkranz, A.; Montaño-Figueroa, A. G.; Arellano-Jiménez, M. J.; Quevedo-Lopez, M.; Valenzuela, P.; Gacitúa, W. Mechanical and microstructural properties of broadband anti-reflective TiO2/SiO2 coatings for photovoltaic applications fabricated by magnetron sputtering. *Sol. Energy Mater. Sol. Cells* **2021**, *220*, 110841.

(36) Callister, W. D. *Fundamentals of materials science and engineering*; Wiley: 2000; Vol. 471660817.

(37) Freund, L. B.; Suresh, S. *Thin film materials: stress, defect formation and surface evolution*; Cambridge University Press: 2004.